

## Numerical Study of the Unsteady Aerodynamics of Freely Falling Plates

Changqiu Jin<sup>1</sup> and Kun Xu<sup>2,\*</sup>

<sup>1</sup> *Institute of Applied Physics and Computational Mathematics, P.O. Box 8009, Beijing 100088, China.*

<sup>2</sup> *Mathematics Department, Hong Kong University of Science and Technology, Hong Kong, China.*

Received 18 July 2007; Accepted (in revised version) 13 September 2007

Available online 11 December 2007

---

**Abstract.** The aerodynamics of freely falling objects is one of the most interesting flow mechanics problems. In a recent study, Andersen, Pesavento, and Wang [J. Fluid Mech., vol. 541, pp. 65-90 (2005)] presented the quantitative comparison between the experimental measurement and numerical computation. The rich dynamical behavior, such as fluttering and tumbling motion, was analyzed. However, obvious discrepancies between the experimental measurement and numerical simulations still exist. In the current study, a similar numerical computation will be conducted using a newly developed unified coordinate gas-kinetic method [J. Comput. Phys, vol. 222, pp. 155-175 (2007)]. In order to clarify some early conclusions, both elliptic and rectangular falling plates will be studied. Under the experimental condition, the numerical solution shows that the averaged translational velocity for both rectangular and elliptical plates are almost identical during the tumbling motion. However, the plate rotation depends strongly on the shape of the plates. In this study, the details of fluid forces and torques on the plates and plates movement trajectories will be presented and compared with the experimental measurements.

**PACS:** 47.11.-j, 47.85.Gj

**Key words:** Navier-Stokes equations, unified coordinate method, unsteady aerodynamics, falling plate.

---

### 1 Introduction

It is an observed fact that not all falling objects travel straight downward under the influence of gravity. For examples, leaves, tree seeds, and paper cards all follow complicated downward trajectories as they fall under gravity. In fact, falling leaves and tumbling sheets of paper often reverse their downward direction, momentarily rising against

---

\*Corresponding author. *Email addresses:* Jin\_changqiu@iapcm.ac.cn (C. Q. Jin), makxu@ust.hk (K. Xu)

gravity, as they flutter or tumble through the air. It is therefore clear that any satisfactory explanation of this complicated natural phenomenon must include a description of the instantaneous fluid forces experienced by the falling object as well as the inertial and gravitational effects that are present.

Previously, only a limited number of analytical results have been proven with reference to objects falling through fluid under gravity, and those that do exist most commonly address only special limits, such as Stokes flow and inviscid irrotational flow. Most falling objects, however, encounter unsteady aerodynamic forces as they fall. As a result, the problem of a rigid body falling through a viscous fluid has recently attracted some attention, especially with the help of computational fluid dynamics. An excellent investigation has been conducted by Pesvento and Wang [13], where in which the governing Navier-Stokes equations were solved numerically in the frame of the falling object.

The fluttering, looping, and tumbling motions have been of interest to physicists since the 19th century, when famed Scottish physicist James Clerk Maxwell studied falling cards and offered a qualitative explanation of the correlation between the sense of rotation and the drift direction of a tumbling card [10], when the classical aerodynamic theory had not been established yet. In the past decades, most investigation only presented qualitative or average properties, such as the phase diagram, where the instantaneous fluid forces were not obtained [2, 4, 5, 14, 15]. Recently, Mittal, Seshadri and Udaykumar (2004) in [11] solved two-dimensional Navier-Stokes equations for a freely falling cylinder. Jones and Shelley [9] suggested a falling card model based on inviscid theory and the unsteady Kutta condition.

Wang and Pesavento [13] studied the aerodynamics of freely falling plates for a quasi two-dimensional flow at Reynolds numbers around  $10^3$ , which is a typical state for a leaf or business card falling in air. They measured the plates trajectories experimentally using a high speed digital video at sufficient resolution and determined the instantaneous plates' acceleration, from which they obtained the instantaneous fluid force and torque on the falling objects. Furthermore, besides the experimental measurements, the direct numerical solutions of the two-dimensional incompressible Navier-Stokes equations for the falling objects have been obtained. The trajectories and forces on the moving plates from both numerical computation and experimental measurement have been qualitatively compared. The discrepancies, such as the falling trajectories and angular velocities, were ascribed to the differences in geometries between the rectangular cross-section in the experiment and the elliptical one in numerical simulation.

In this study, we will investigate the motion of freely falling plates numerically using a newly developed gas-kinetic scheme, in which the governing Navier-Stokes equations are solved on a moving grid. In the computations that follow, the grid will be fixed to the falling plate and so the motion of the grid itself will be determined by the translational and rotational motion of the plate. Similar to the Lagrangian method, each grid will follow its own grid velocity during a time step, but the flow update in the whole computational domain around the falling plate is in a common inertial reference frame. Therefore, there will be no additional forces related to the non-inertial frame of ref-

erence in the current computation. Besides simulating the elliptic falling plate studied by Pesavento and Wang [13], we will also consider a rectangular plate that has the same cross-section as that used in the experiment. In each case, the instantaneous fluid forces on the falling plate will be quantitatively evaluated and compared with the experimental measurements of Andersen, Pesavento, and Wang [1]. Based on the current study, some discrepancies between the experimental measurements and numerical computations in the early investigation by Andersen et al. [1], such as the plate trajectory, and fluid forces and torques on the plate, will be resolved.

## 2 Unified coordinate method for viscous flow

The Bhatnagar-Gross-Krook (BGK) model of the approximate Boltzmann equation in two dimensional space is given by [3],

$$f_t + u f_x + v f_y = \frac{g - f}{\tau}, \quad (2.1)$$

where  $f$  is the gas distribution function,  $\tau$  is the particle collision time, and  $g$  is the equilibrium state approached by  $f$ . Both  $f$  and  $g$  are functions of space  $(x, y)$ , time  $t$ , particle velocity  $(u, v)$ , and internal variable  $\zeta$ . With the grid movements, a unified coordinate transformation from the physical domain  $(t, x, y)$  to the computational domain  $(\lambda, \xi, \eta)$  is used [6, 7],

$$\begin{aligned} dt &= d\lambda, \\ dx &= U_g d\lambda + A d\xi + L d\eta, \\ dy &= V_g d\lambda + B d\xi + M d\eta, \end{aligned} \quad (2.2)$$

where  $(U_g, V_g)$  are the grid velocity, and  $(A, B, L, M)$  are the geometrical variables, such as  $A = \partial x / \partial \xi$  and  $L = \partial x / \partial \eta$ , which can be updated through the geometric conservative laws,

$$\frac{\partial A}{\partial \lambda} = \frac{\partial U_g}{\partial \xi}, \quad \frac{\partial B}{\partial \lambda} = \frac{\partial V_g}{\partial \xi}, \quad \frac{\partial L}{\partial \lambda} = \frac{\partial U_g}{\partial \eta}, \quad \frac{\partial M}{\partial \lambda} = \frac{\partial V_g}{\partial \eta}.$$

With the above transformation (2.2), the gas-kinetic BGK equation becomes

$$\begin{aligned} & \frac{\partial}{\partial \lambda} (\Delta f) + \frac{\partial}{\partial \xi} \left\{ [(u - U_g)M - (v - V_g)L] f \right\} + \frac{\partial}{\partial \eta} \left\{ [-(u - U_g)B + (v - V_g)A] f \right\} \\ &= \frac{g - f}{\tau} \Delta, \end{aligned} \quad (2.3)$$

where  $\Delta = AM - BL$  is the Jacobian of the transformation.

For an equilibrium flow with a gas distribution  $f = g$ , by taking the conservative moments

$$\phi = (1, u, v, \frac{1}{2}(u^2 + v^2 + \zeta^2))^T$$

to Eq. (2.3), the corresponding inviscid governing equations under the mesh movement in the inertial Eulerian space can be obtained [8]. Based on the Chapman-Enskog expansion, up to the 1st order of  $\tau$ , the gas distribution function becomes

$$f = g - \frac{\tau}{\Delta} \left( \frac{\partial}{\partial \lambda} (\Delta g) + \frac{\partial}{\partial \xi} \{ [(u - U_g)M - (v - V_g)L]g \} + \frac{\partial}{\partial \eta} \{ [-(u - U_g)B + (v - V_g)A]g \} \right).$$

Taking moments  $\phi$  again in Eq. (2.3) with the above gas distribution function, the Navier-Stokes equations can be obtained.

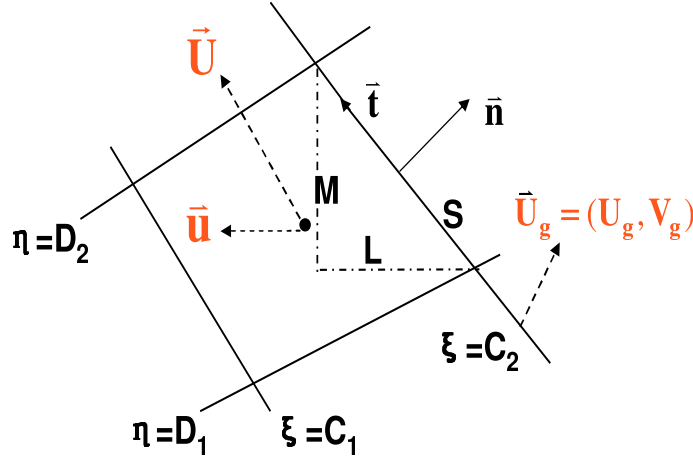


Figure 1: Schematic configuration around a moving cell interface.

Numerically, we solve the gas-kinetic equation for the viscous flow using a direction by direction splitting method. The BGK model (2.3) in the  $\xi$ -direction is,

$$\frac{\partial}{\partial \lambda} (\Delta f) + \frac{\partial}{\partial \xi} \{ [(u - U_g)M - (v - V_g)L]f \} = \frac{g - f}{\tau} \Delta. \quad (2.4)$$

For a finite volume scheme, at a moving interface  $\xi = \text{constant}$ , the normal and tangent directions are defined by

$$\bar{n} = \nabla \xi / |\nabla \xi| = (M, -L) / S, \quad \bar{t} = (L, M) / S,$$

where  $S = \sqrt{M^2 + L^2}$  is the physical length of the cell interface, see Fig. 1 for the schematic configuration. The particle velocities relative to the moving cell interface are  $(u - U_g, v - V_g)$ , which can be decomposed into normal  $\tilde{u}$  and tangential  $\tilde{v}$  velocities,

$$\begin{aligned} \tilde{u} &= (u - U_g)M/S - (v - V_g)L/S, \\ \tilde{v} &= (u - U_g)L/S + (v - V_g)M/S. \end{aligned} \quad (2.5)$$

Hence, Eq. (2.4) in the  $\xi$ -direction becomes

$$\frac{\partial}{\partial \lambda} (\Delta f) + \frac{\partial}{\partial \xi} (S \tilde{u} f) = \frac{g - f}{\tau} \Delta.$$

The above equation is numerically solved to evaluate a gas distribution function  $f$  at the moving cell interface  $\zeta = \text{constant}$ , and subsequently obtain the numerical fluxes. In the above equation,  $\Delta$  is the area of the computational cell in the physical space, and  $S$  is the length of the cell interface. Therefore, the above equation is equivalent to

$$\frac{\partial}{\partial \lambda}(f) + \frac{\partial}{\partial \tilde{x}}(\tilde{u}f) = \frac{g-f}{\tau}, \tag{2.6}$$

where  $\tilde{x}$  is the length scale in the normal direction of the moving cell interface in the physical space. Eq. (2.6) is the BGK model in the local moving frame of reference, which can be solved numerically using the BGK-NS method [16]. For the low speed incompressible flow, the gas distribution function at a cell interface can be simplified to [17],

$$f(\zeta_{i+1/2}, \eta_j, t, \tilde{u}, \tilde{v}, \zeta) = g_0(1 - \tau(a\tilde{u} + A) + At), \tag{2.7}$$

where  $g_0$  is the equilibrium state at the moving cell interface and  $-\tau(a\tilde{u} + A)g_0$  is the corresponding non-equilibrium part for the viscous terms. Therefore, standing on the moving cell interface, the fluxes can be explicitly evaluated,

$$\begin{bmatrix} \mathcal{F}_\rho \\ \mathcal{F}_{\rho\tilde{u}} \\ \mathcal{F}_{\rho\tilde{v}} \\ \mathcal{F}_{\tilde{E}} \end{bmatrix}_{i+1/2,j} = \int \tilde{u} \begin{bmatrix} 1 \\ \tilde{u} \\ \tilde{v} \\ \frac{1}{2}(\tilde{u}^2 + \tilde{v}^2 + \zeta^2) \end{bmatrix} f(\zeta_{i+1/2}, \eta_j, t, \tilde{u}, \tilde{v}, \zeta) d\Xi. \tag{2.8}$$

Since the local cell interface is moving with a constant translational velocity, the above fluxes are still in the inertial reference of frame. Since different numerical cells move with different grid velocities, in order to update the flow variables in the whole computational domain, we have to update the conservative variables of each cell in a commonly defined Eulerian space. Therefore, we need to translate the above fluxes in Eq. (2.8) standing on the moving cell interface into the fluxes for the mass, momentum and energy transport in the common inertia frame of reference, the so-called inertial physical space which is not moving with the falling plate. So, the mass, momentum, and energy transport in the Eulerian space across the cell interface  $\zeta = \text{Constant}$  are calculated by

$$\begin{bmatrix} F_\rho \\ F_m \\ F_n \\ F_E \end{bmatrix}_{i+1/2,j} = \int S\tilde{u} \begin{bmatrix} 1 \\ u \\ v \\ \frac{1}{2}(u^2 + v^2 + \zeta^2) \end{bmatrix} f(\zeta_{i+1/2}, \eta_j, t, \tilde{u}, \tilde{v}, \zeta) d\Xi, \tag{2.9}$$

where  $S$  is the length of the cell interface. In order to evaluate the above flux integration, the easiest way is to write the  $(u, v)$  velocities in terms of  $(\tilde{u}, \tilde{v})$ . Based on the transformation (2.5), we have

$$u = U_g + \frac{M\tilde{u} + L\tilde{v}}{S}, \quad v = V_g + \frac{-L\tilde{u} + M\tilde{v}}{S}.$$

Therefore, Eq. (2.9) becomes

$$\begin{bmatrix} F_\rho \\ F_m \\ F_n \\ F_E \end{bmatrix}_{i+1/2,j} = \begin{bmatrix} S\mathcal{F}_\rho \\ M\mathcal{F}_{\rho\bar{u}} + L\mathcal{F}_{\rho\bar{v}} + SU_g\mathcal{F}_\rho \\ -L\mathcal{F}_{\rho\bar{u}} + M\mathcal{F}_{\rho\bar{v}} + SV_g\mathcal{F}_\rho \\ (MU_g - LV_g)\mathcal{F}_{\rho\bar{u}} + (LU_g + MV_g)\mathcal{F}_{\rho\bar{v}} + S\mathcal{F}_{\bar{E}} + \frac{S}{2}(U_g^2 + V_g^2)\mathcal{F}_\rho \end{bmatrix}, \quad (2.10)$$

where  $(\mathcal{F}_\rho, \mathcal{F}_{\rho\bar{u}}, \mathcal{F}_{\rho\bar{v}}, \mathcal{F}_{\bar{E}})$  are given in Eq. (2.8).

With the above fluxes, the conservative flow variables can be updated in each moving computational cell by

$$Q_{i,j}^{n+1} = Q_{i,j}^n + \frac{1}{\Delta\bar{\xi}} \int_{t^n}^{t^{n+1}} (\mathbf{F}_{i-1/2,j} - \mathbf{F}_{i+1/2,j}) dt + \frac{1}{\Delta\eta} \int_{t^n}^{t^{n+1}} (\mathbf{G}_{i,j-1/2} - \mathbf{G}_{i,j+1/2}) dt,$$

where

$$Q = (\rho\Delta, \rho\Delta U, \rho\Delta V, \rho\Delta E)^T$$

is the total mass, momentum and energy inside each cell and  $\mathbf{F} = (F_\rho, F_m, F_n, F_E)^T$  is given in Eq. (2.10). The flux in the  $\eta$ -direction is denoted by  $\mathbf{G}$ , which can be constructed similarly.

The only free parameter in the above flux functions is the particle collision time, i.e.,  $\tau$ , which is related to the departure of a gas distribution function away from the equilibrium state (2.7). Based on the Chapman-Enskog expansion, the relation between the particle collision time and the flow dissipative coefficient is the following,

$$\tau = \mu / p,$$

where  $\mu$  is the dynamic viscosity coefficient and  $p$  is the local pressure. For a flow problem, once the Reynolds number is given, i.e.,  $Re = \rho UL / \mu$ , the particle collision time will be uniquely determined locally. Since all simulations presented in this paper are for smooth flows, the truncation error of the current scheme is  $\mathcal{O}(\tau(\Delta t)^2)$  [12]. For high Reynolds number flow simulation, the collision time can be much less than the time step  $\Delta t$ . Therefore, the current method is a high order accurate numerical scheme.

### 3 Falling plates movement inside a viscous fluid

The falling plate movement inside a viscous fluid can be only described by solving a coupled system of the Navier-Stokes equations for the fluid and Newton's law for the solid plate. Based on the fluid solution, the pressure and viscous forces as well as the torque on the plate can be explicitly evaluated. Since the computational mesh is fixed on the falling plate, the mesh velocity can be computed according to the translational and rotational movement of the plate. The viscous fluid solution around the moving plate is calculated using the moving mesh method in the last section.

### 3.1 Parameterizations of the plate and integration of forces

A freely falling plate is characterized by six dimensional parameters: the width  $l$ , the thickness  $h$ , the density  $\rho_b$  of the plate, the density  $\rho_f$  of the fluid, the kinematic viscosity  $\nu$  of the fluid, and the gravitational acceleration  $G$ . Based on the above six dimensional numbers, three non-dimensional numbers, i.e., the thickness to width ratio,  $\beta$ , the dimensionless moment of inertia,  $I^*$ , and the Reynolds number,  $Re$ , can be defined. Following the same method used in [13], the parameters defined include:

- the ratio between the thickness and width of the plate,

$$\beta = h/l;$$

- the dimensional moment of inertia  $I$  and dimensionless moment of inertia  $I^*$  of the elliptical plate,

$$I = \frac{\pi l h (l^2 + h^2) \rho_b}{64}, \quad I^* = \frac{h (l^2 + h^2) \rho_b}{2 l^3 \rho_f},$$

and the rectangular plate,

$$I = \frac{l h (l^2 + h^2) \rho_b}{12}, \quad I^* = \frac{8 h (l^2 + h^2) \rho_b}{3 \pi l^3 \rho_f};$$

- the Reynolds number

$$Re = u_t l / \nu,$$

where  $l$  is the length of the plate and  $u_t$  is the terminal velocity which is estimated by balancing gravity against the fluid force on a plate with the drag coefficient equal to 1. The terminal velocities are

$$u_t = \sqrt{\frac{\pi h g}{2} \left( \frac{\rho_b}{\rho_f} - 1 \right)}$$

for the elliptical plate and

$$u_t = \sqrt{2 h g \left( \frac{\rho_b}{\rho_f} - 1 \right)}$$

for the rectangular plate.

The fluid forces on the plate include pressure force and viscous force. These quantities can be calculated by integrating along the plate surface explicitly once the fluid solution is obtained around the falling plate. In the following, we will calculate the fluid forces and torque for both moving elliptic and rectangular plates through the integration of surface forces. The pressure force can be written as an integral of the pressure over the boundary  $\Gamma$  of the body,

$$\vec{F}_p = - \oint_{\Gamma} p \vec{n} ds = - \oint_{\Gamma} p (\cos \theta, \sin \theta) ds = - \oint_{\Gamma} (p_x, p_y) ds, \quad (3.1)$$

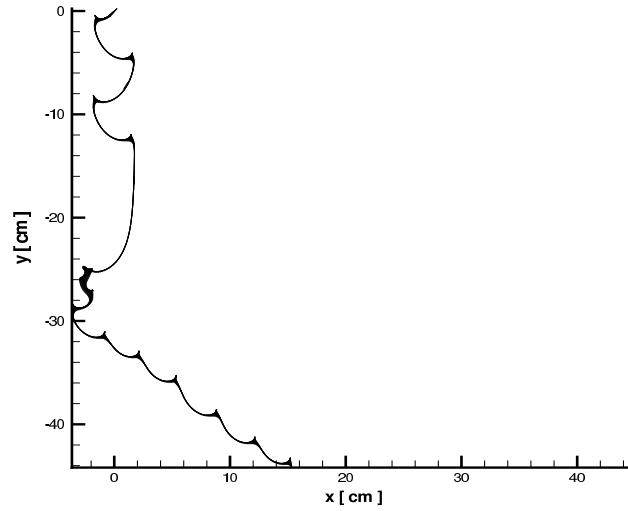


Figure 2: Falling trajectory of a rectangle from fluttering to tumbling motion.

where  $p$  is the pressure,  $\vec{n} = (\cos\theta, \sin\theta)^T$  is the normal direction of  $ds$ , and  $s$  is the arc length along the boundary. Numerically, Eq. (3.1) becomes,

$$\vec{F}_p = - \left( \sum_i p_i \cos\theta \Delta s_i, \sum_i p_i \sin\theta \Delta s_i \right) = (P_x, P_y),$$

where  $i$  stands for the  $i$ th grid on the moving boundary, and  $\Delta s_i$  is the length of the  $i$ th cell interface on the surface of the plate. The total pressure force is decomposed into  $P_x$  along the  $x$ -direction and  $P_y$  along the  $y$ -direction in the inertia frame of reference.

The viscous force is obtained by integrating the stress  $\mu \partial U_t / \partial n$ ,

$$\begin{aligned} \vec{F}_v &= - \oint_{\Gamma} \mu \frac{\partial U_t}{\partial n} \vec{t} ds \\ &= - \oint_{\Gamma} \mu \frac{\partial U_t}{\partial n} (-\sin\theta, \cos\theta) ds = - \oint_{\Gamma} (v_x, v_y) ds, \end{aligned} \tag{3.2}$$

where  $\vec{t} = (-\sin\theta, \cos\theta)^T$  is the tangent direction of  $ds$ ,  $U_t = \vec{U} \cdot \vec{t}$  is the velocity in the tangential direction, and  $\mu$  is the dynamic viscosity coefficient. Numerically, Eq. (3.2) is solved by

$$\vec{F}_v = - \left( \sum_i v_i \cos\theta \Delta s_i, \sum_i v_i \sin\theta \Delta s_i \right) = (v_x, v_y).$$

The viscous force is decomposed into  $v_x$  along the  $x$ -direction and  $v_y$  along the  $y$ -direction.

The pressure torque is also obtained by the following integrating along the surface of a falling plate,

$$\begin{aligned} \tau_p &= \oint_{\Gamma} \vec{r} \times (-p\vec{n}) ds \\ &= \sum_i \vec{r}_i \times (-p_i \vec{n}) \Delta s_i = \sum_i [x_i (p_y)_i - y_i (p_x)_i], \end{aligned}$$



where  $\vec{r}_i = (x_i - x_c, y_i - y_c)$  is the vector from the geometrical center  $(x_c, y_c)$  of the plate to the center of the  $i$ th grid  $(x_i, y_i)$  on the plate surface. Similarly, the viscous torque can be calculated by

$$\begin{aligned}\tau_v &= \oint_{\Gamma} \vec{r} \times \mu \frac{\partial U_t}{\partial n} \vec{t} ds \\ &= \sum_i \vec{r}_i \times \mu \frac{\partial U_t}{\partial n} \vec{t} \Delta s_i = \sum_i [x_i(v_y)_i - y_i(v_x)_i].\end{aligned}$$

So far, the pressure and viscous forces and their torques have been obtained on a plate. The buoyancy corrected gravitational force  $\vec{F}_g$  on the plate in the negative  $y$ -direction becomes

$$\vec{F}_g = -\frac{\pi l h (\rho_b - \rho_f) G}{4},$$

for the elliptical plate, and

$$\vec{F}_g = -l h (\rho_b - \rho_f) G,$$

for the rectangular one. The total force  $\vec{F}$  is equal to the summation of the pressure force  $\vec{F}_p$ , viscous force  $\vec{F}_v$ , and the buoyancy corrected gravitational force  $\vec{F}_g$ , namely,

$$\vec{F} = \vec{F}_p + \vec{F}_v + \vec{F}_g.$$

Furthermore, the total force  $\vec{F}$  can be decomposed into  $F_x$  in the  $x$ -direction and  $F_y$  in the  $y$ -direction,

$$\vec{F} = (F_x, F_y) = (P_x + v_x, P_y + v_y + F_g).$$

Similarly, the total torque includes the torques due to the pressure and viscous force  $\tau = \tau_p + \tau_v$ .

Let  $\vec{a} = (a_x, a_y)$  and  $\vec{\Omega}$  be the translational and the angular acceleration of the plate, which are related to the force and torque on the plate through Newton's law,

$$F_x = m a_x, \quad F_y = m a_y, \quad \tau = I d\Omega / dt.$$

Due to the plate translational and rotational movement, the grid velocity  $\vec{U}$  between two subsequent time steps at the center of a computational cell is given by

$$\vec{U}^{n+1} = \vec{U}^n + \Delta t^n \vec{a} + \Delta t^n \vec{r} \times \vec{\Omega},$$

where  $\vec{r}$  is the vector from the geometric center of the plate to the center of the numerical cell. The above velocity is fed back into the moving mesh method as the grid velocity  $(U_g, V_g)$ .

Even though the grid of the whole computational domain is fixed to the plate and moving with the plate's movement, within each time step the grid velocity for each cell is set to be a constant. Certainly, different cells have different velocities. Therefore, the

local moving frame of reference is still an inertial one and the forces associated with the non-inertial reference of frame will not appear. Since the updated flow variables inside each computational cell are defined relatively to a commonly referenced inertial frame, such as the water tank in the laboratory, the boundary conditions are constructed by assigning conservative flow variables in the ghost cells. For the out boundary, the flow variables inside the ghost cells are set up using the Riemann invariants, and the fluid in the infinity is considered to have zero velocity. For the boundary around the moving plate, the fluid variables in the ghost cells are assigned to keep the averaged fluid velocity on the plate surface being equal to the plate movement velocity, i.e., the so-called no-slip boundary condition.

### 3.2 Unsteady falling plates movements

In the two-dimensional experiment conducted by Andersen, Persavento, and Wang [1], a small rectangular aluminum plate was designed to fall freely in a water tank. For the falling plate, many physical quantities were measured, such as the plate trajectory and falling speed. The fluid force and torque on the plate were calculated according to the experimental data. Here, following the experiment, we apply the above moving mesh method to solve the two dimensional Navier-Stokes equations to study the rich dynamical behavior of falling plates. In the following, we simulate the plate movement under the following conditions:  $\beta = 1/8$ ,  $h = 0.081\text{cm}$ ,  $\rho_f = 1.0\text{gcm}^{-3}$ ,  $\rho_b = 2.7\text{gcm}^{-3}$ , and  $\rho_b/\rho_f = 2.7$ . In the current simulations, the Reynolds numbers for ellipse and rectangle are  $Re = lu_t/\nu = 1100$  and  $837$  respectively. The radius of the computational domain has a value about five times the length of the longer axis of the plate, i.e.,  $r = 5L$  and  $L$  is the chord length. In order to confirm the convergence of the computational results, a large domain with  $r = 10L$  is also used. In both cases, two stretched meshes are generated around the falling plates with  $200 \times 50$  and  $400 \times 100$  grid points separately. Since the solution close to the plate is well resolved by the small cell size and different mesh stretching parameters are used, the simulation results on different computational domain basically capture mesh refinement effects.

In the early investigations [1, 13], due to the limitation of their numerical method, in order to avoid the singularities at the corners of a rectangular plate, a plate with elliptic cross-section was used in the numerical computation even though a rectangular one was used in the experiment. Since the current numerical method has no constraint on the falling plate geometry, hence we will conduct the computations for plates with both elliptic and rectangular cross-sections. In other words, the current study essentially tries to resolve the discrepancy presented in early investigation by performing the missing computation using a plate of rectangular cross-section. Also, the validity of the early computation will be tested.

Firstly, we present the simulation result for the elliptic plate. Fig. 3 shows the computational mesh around an elliptic plate with an initial angle of  $0.2$  radian with respect to the horizontal axis. Fig. 6 presents two representative trajectories of the falling plate,

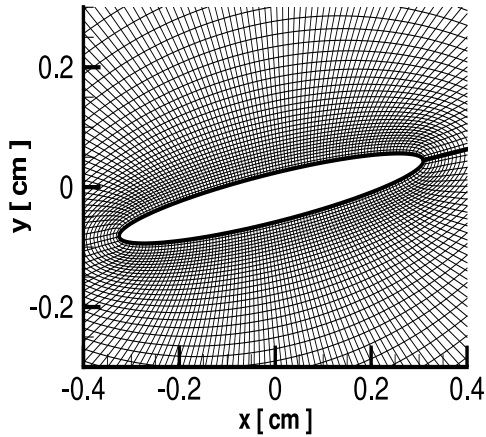


Figure 3: Computational grid around the ellipse.

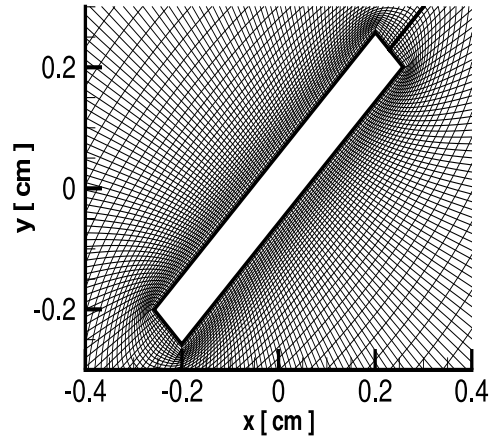


Figure 4: Computational grid around the rectangle.

Table 1: Experimental and numerical falling plate averaged translational and angular velocities.

		U [cm/s]	V [cm/s]	$\omega$ [rad/s]
Experiment (Andersen et al. [1])		$15.9 \pm 0.3$	$-11.5 \pm 0.5$	$14.5 \pm 0.3$
Computations	Ellipse	$15.3 \pm 0.05$	$-11.2 \pm 0.16$	$16.9 \pm 0.01$
	Rectangle	$15.1 \pm 0.30$	$-11.8 \pm 0.37$	$15.0 \pm 0.36$

where the black one is the experimental measurement in [1] and the purple one is the trajectory from our computation. Overall, the two trajectories are very close to each other and have almost the same slope, but with obvious phase differences. In other words, under the current flow condition the geometrical differences between the ellipse (numerics) and rectangle (experiment) will not effect much on the plate falling velocities, but they will severely effect the rotation or angular velocity of the plates. Obviously, due to the smooth profile of the elliptical plate, its angular velocity is much faster than that of the rectangular plate. The quantitative falling velocity in the  $x$ - and  $y$ -directions, as well as angular velocity are listed in Table 1. Except for the angular velocity, the averaged translational velocities between the experimental measurement ( $V_x = 15.9 \text{ cm/s}, V_y = -11.5 \text{ cm/s}$ ) and the numerical computation ( $V_x = 15.3 \text{ cm/s}, V_y = -11.8 \text{ cm/s}$ ) match reasonably. This observation is different from the numerical solutions ( $V_x = 15.6 \text{ cm/s}, V_y = -7.4 \text{ cm/s}$ ) in [1, 13], where the  $y$ -direction velocity seems too small in comparison with the experimental measurement. Andersen, Persavento, and Wang attributed this discrepancy to the geometrical differences between the experimental rectangle and numerical ellipse. Based on the current computation, it seems that their difference in the  $y$ -direction velocities may be due to the numerical algorithm.

The vorticity field at four instants during a full rotation of the elliptical plate is presented in Fig. 5. The vorticity field is similar to the numerical one reported in [13]. As presented in the last section, the kinetic scheme is a finite volume conservative method.

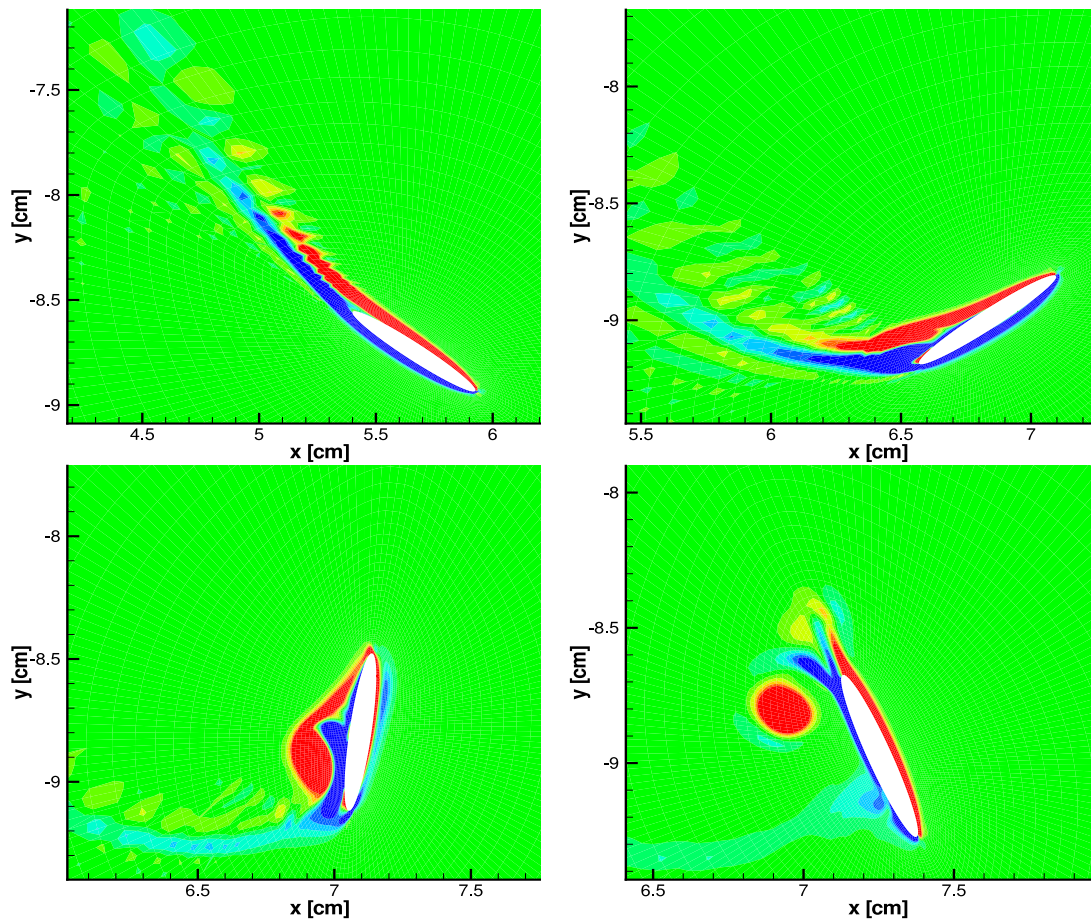


Figure 5: Vorticity field around a falling ellipse at four instants during a full rotation.

The updated flow variables are the mass and momentum densities inside each computational cell. The vorticity field in our case is numerically obtained by the direction-by-direction discretization of the velocity field. The velocity field is pretty smooth in our case and the noise in the vorticity distribution is due to our method to calculate it. The method in [13] directly updates the vorticity flow variable. In Fig. 8, the instantaneous fluid forces are also plotted, where the red one is the total fluid force on the plate, the green one is the pressure force, and the blue one is the viscous force. The constant buoyancy corrected gravitational force  $m'G$ , i.e.,  $m' = (\rho_b - \rho_f)\pi lh/4$ , is not included there. Fig. 8 clearly shows that the viscous force is always in the opposite direction of the elliptic plate movement except at the singular turning point.

Following the experimental strategy, the rectangle plate is released at an initial angle of  $0.25\pi$  radian with respect to the horizontal axis, with an initial velocity  $U = (-8.92\text{cm/s}, -8.92\text{cm/s})$ . The computational grid around the rectangle is shown in Fig. 4. For the rectangular plate, the plate motion is much more complicated than that of the

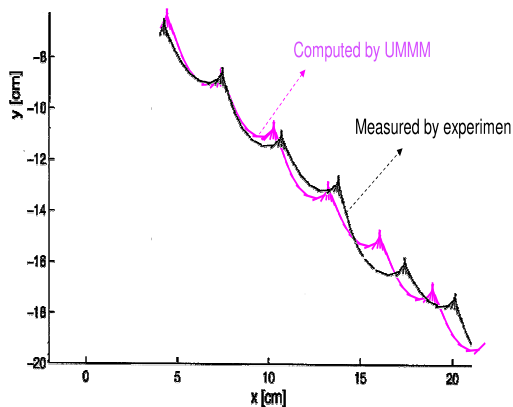


Figure 6: Trajectories of falling ellipse: experiment (black) and computation (purple).

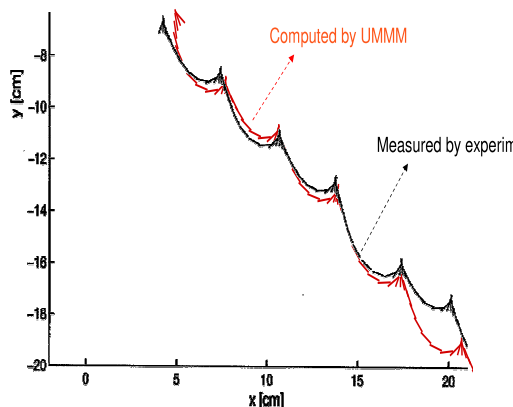


Figure 7: Trajectories of the falling rectangle in the tumbling section: experiment (black) and computation (red).

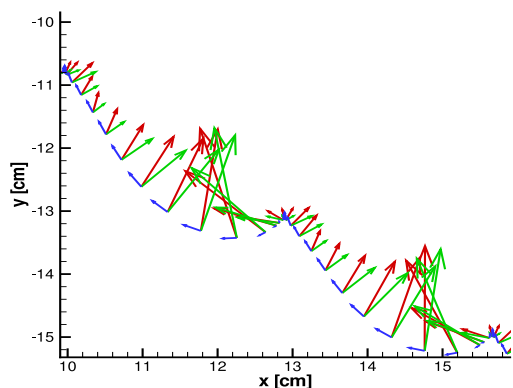


Figure 8: Fluid forces on the ellipse in the tumbling process: total fluid force (red), pressure force (green), and viscous force (blue).

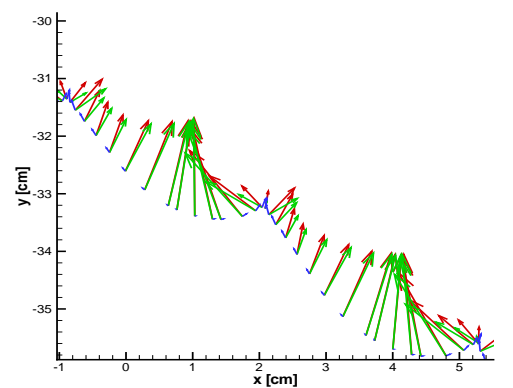


Figure 9: Fluid forces on the rectangle: total fluid force (red), pressure force (green), and viscous force (blue).

ellipse, see Fig. 2 for the trajectory. For example, with the above initial condition, the rectangular plate first has a fluttering motion from side to side, then after a while it starts to tumble. Since the experimental results presented in [1] were for the tumbling section, the numerical data in the corresponding section is extracted and compared with the experimental data. Fig. 7 shows the rectangular plate trajectory of the current simulation and experimental measurement [1]. From this figure, the improvement of the rotational velocity of the plate can be clearly identified. Quantitatively, the averaged  $x$ - and  $y$ -direction velocity components become  $(V_x = 15.1\text{cm/s}, V_y = -11.8\text{cm/s})$ , and the angular velocity is  $(\omega = 15.0\text{rad/s})$ , which have an excellent match with the experimental results, especially for the angular velocity. Due to the rectangular shape, the rotational speed becomes much slower than that for the elliptical one. The vorticity field at four instants during a full rotation is presented in Fig. 11, which behaves more violent and unsteady

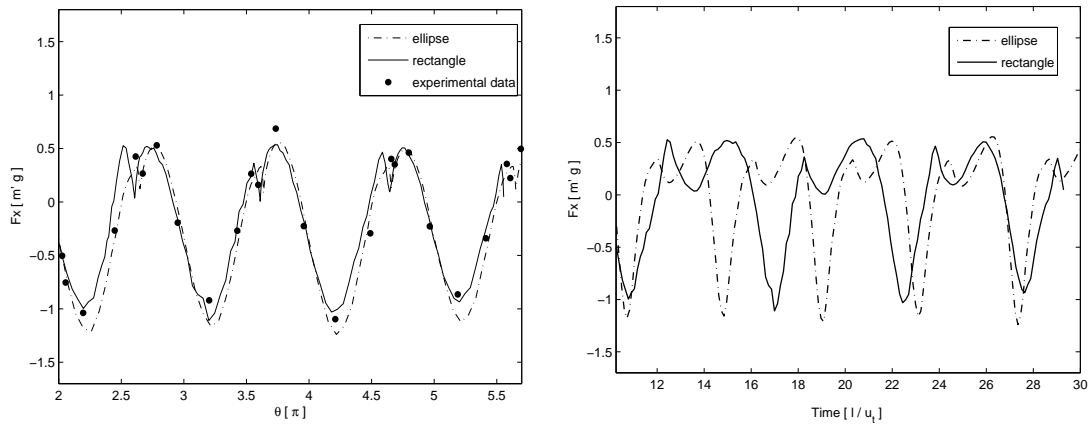


Figure 10:  $x$ -direction fluid force  $F_x$  on the plate during the tumbling process for both ellipse and rectangle. The horizontal axis are rotational angle (left) and dimensionless time (right).

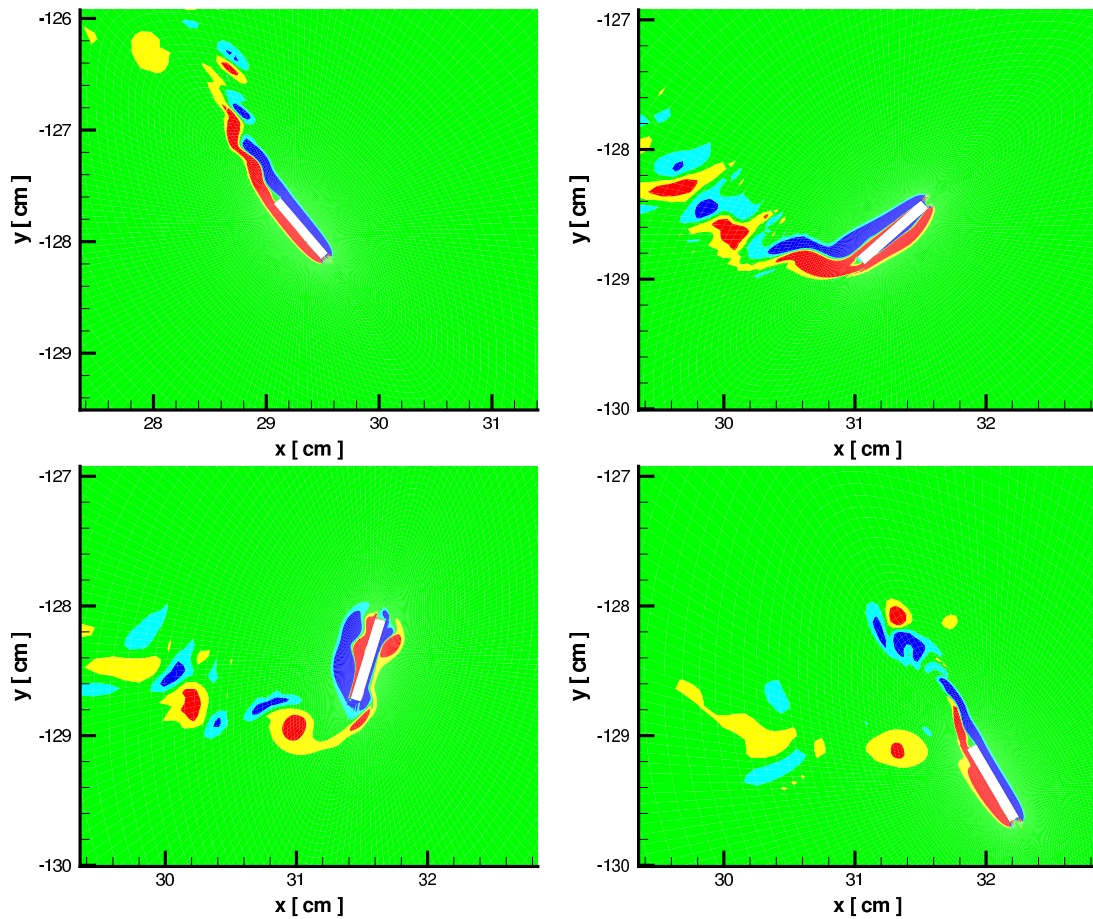


Figure 11: Vorticity field of a falling rectangle at four instants during a full rotation.

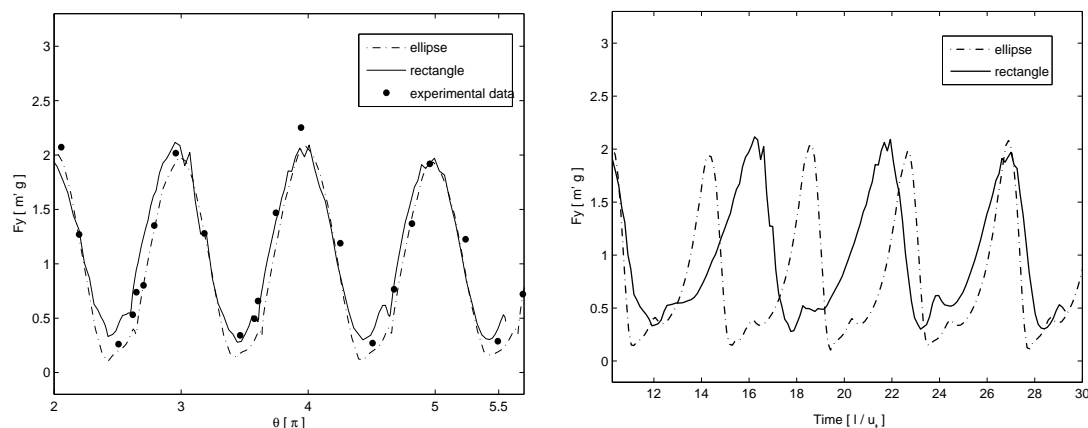


Figure 12:  $y$ -direction fluid force  $F_y$  on the plate during the tumbling process for both ellipse and rectangle. The horizontal axis are rotational angle (left) and dimensionless time (right).

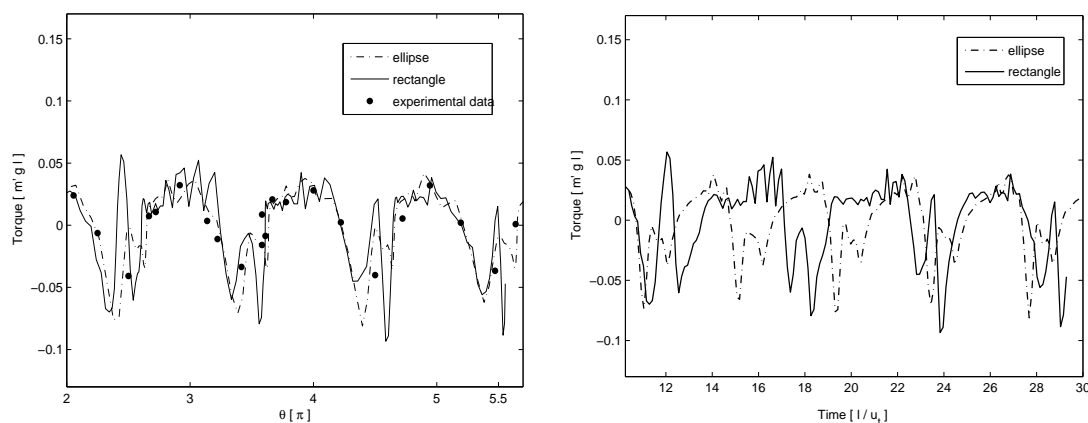


Figure 13: Torques on the plate during the tumbling process for both ellipse and rectangle. The horizontal axis are rotational angle (left) and dimensionless time (right).

than the corresponding one in the elliptic case. For example, the flow separation point around the rectangle is much close to the leading edge of the plate. Fig. 9 shows the instantaneous fluid forces on the plate, where the red one is the total fluid force, the green one is the pressure force, and the blue one is viscous force.

Besides the magnitude differences of the viscous forces on the elliptical and rectangular plates, see Figs. 8 and 9, the interesting phenomenon is the direction of the viscous force, especially during the plate upward movement. For the elliptical plate, the viscous force is always in the opposite direction of the plate movement. However, for the rectangular one, due to the separation and unsteadiness, during the short upward flight, the viscous force can become a driving force for the moving plate even with a very small magnitude. During the upward rising period, the separated fluid around the plate moves faster than the plate itself. Also, the numerical observation shows that the total pressure

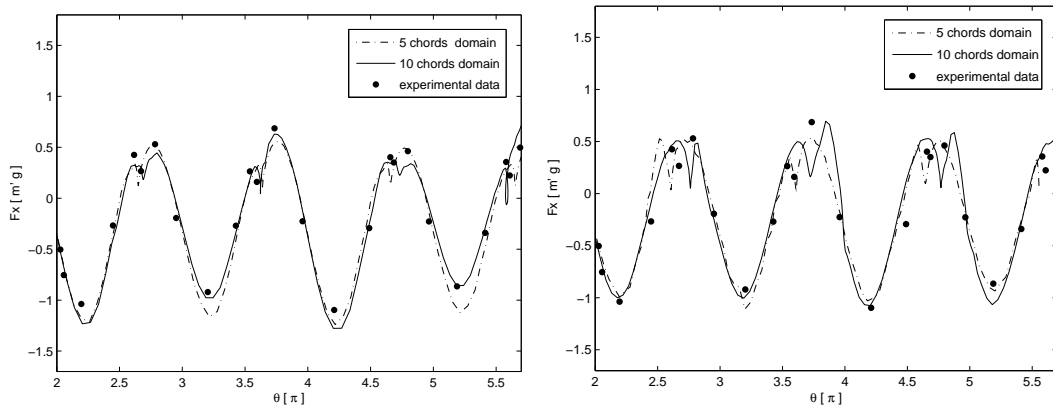


Figure 14: Comparison of the  $F_x$  force from two computations with different computational domain, i.e., 5 and 10 chord lengths, for falling ellipse (left) and rectangle (right).

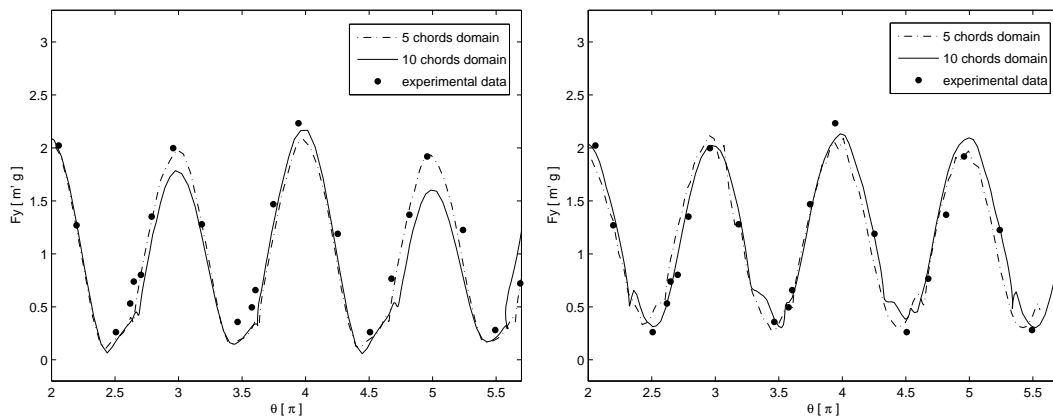


Figure 15: Comparison of the  $F_y$  force from two computations with different computational domain, i.e., 5 and 10 chord lengths, for falling ellipse (left) and rectangle (right).

force on the elliptic plate is almost perpendicular to the long axis of the plate. However, for the rectangular one the pressure force can be tilted relative to the long symmetric axis of the plate due to the two small sections at the two ends of the rectangle plate. Based on the numerical computations, Figs. 10-13 present the components of the fluid forces and their torque as a function of the plate orientation (phase) and evolution time respectively. In Fig. 10, the horizontal axis of the left plot is the angle of the tumbling plate. However, the horizontal axis of the right plot uses the real evolution time. The phase error in the plates movement can be clearly observed from the right plot. From these figures, reasonable agreements between the experimental data [1] and the current numerical solutions are obtained. The elliptic plate rotates much faster than the rectangular one. Based on the simulations, we basically agree with the conclusion in Mittal et al's paper. Firstly, computations show that the moment for rotation is mainly from the pressure and not the shear



stress. This can be seen in the different magnitude of the pressure and stress forces, especially for the rectangular case. Secondly, the moment on the plate is produced primarily by low pressure on the leeward side of the plate due to the shedding of vortices.

In order to clarify the boundary effect on the numerical solution, a large computational domain with a radius of 10 times the chord length has also been used to repeat the above computation. The fluid forces from both computations are presented in Figs. 14-15. Basically, both results are close to each other. The forces with a larger computational domain are slightly closer to the experimental measurements.

## 4 Conclusion

In this paper, we investigate the aerodynamics of freely falling plates using a newly developed moving mesh method for the Navier-Stokes equations. During the tumbling movement, the plate trajectory, fluid force, and translational and angular velocities are extracted and compared with the experimental measurements. Good agreements between them are obtained. The current investigation clarifies some discrepancies between the experimental data and the numerical computations in an early study by Andersen, Persavento, and Wang [1]. For example, the current study shows that the plate falling velocity and trajectory are almost the same for the elliptical and rectangular plates under the experimental condition in [1]. The main dynamical differences due to the geometrical shapes are the angular velocity, where the rectangular plate rotates much slower than the elliptical plate. Overall, for the falling plate problem, the fluid dynamics associated with the unsteadiness of the flow and these shed vortices as well as its subsequent effect on the motion of the object can be complex enough to make theoretical treatment difficult. The numerical simulation becomes an indispensable tool, from which the rich unsteady aerodynamics in the whole flight process can be extracted.

## Acknowledgments

The work described in this paper was substantially supported by grants from the Research Grants Council of the Hong Kong Special Administrative region, China (Project No. HKUST6210/05E and 6214/06E).

## References

- [1] A. Andersen, U. Persavento and Z. J. Wang, Unsteady aerodynamics of fluttering and tumbling plates, *J. Fluid Mech.*, 541 (2005), 65-90.
- [2] A. Belmonte, H. Eisenberg and E. Moses, From flutter to tumble: Inertial drag and Froude similarity in falling paper, *Phys. Rev. Lett.*, 81 (1998), 345-348.
- [3] P. L. Bhatnagar, E. P. Gross and M. Krook, A model for collision processes in gases I: Small amplitude processes in charged and neutral one-component systems, *Phys. Rev.*, 94 (1954), 511-525.

- [4] P. Dupleich, Rotation in free fall of rectangular wings of elongated shape, NACA Technical Memo, 1201 (1941), 1-99.
- [5] S. B. Field, M. Klaus, M. G. Moore and F. Nori, Chaotic dynamics of falling disks, *Nature*, 388 (1997), 252-254.
- [6] W. H. Hui, The unified coordinate system in computational fluid dynamics, *Commun. Comput. Phys.*, 2 (2007), 577-610.
- [7] W. H. Hui, P. Y. Li and Z. W. Li, A unified coordinated system for solving the two-dimensional Euler equations, *J. Comput. Phys.*, 153 (1999), 596-637.
- [8] C. Q. Jin and K. Xu, A unified moving grid gas-kinetic method in Eulerian space for viscous flow computation, *J. Comput. Phys.*, 222 (2007), 155-175.
- [9] M. A. Jones and M. J. Shelley, Falling cards, *J. Fluid Mech.*, 540 (2005), 393-425.
- [10] J. C. Maxwell, *The Scientific Papers of James Clerk Maxwell*, Dover, New York, 1890, pp. 115-118.
- [11] R. Mittal, V. Seshadri and H. S. Udaykumar, Flutter, tumble and vortex induced autorotation, *Theor. Comp. Fluid Dyn.*, 17 (2004), 165-170.
- [12] T. Ohwada, On the construction of kinetic schemes, *J. Comput. Phys.*, 177 (2002), 156-175.
- [13] U. Pesavento and Z. J. Wang, Falling paper: Navier-Stokes solutions, model of fluid forces, and center of mass elevation, *Phys. Rev. Lett.*, 93(14) (2004), 144501.
- [14] E. H. Smith, Autorotating wings: An experimental investigation, *J. Fluid Mech.*, 50 (1971), 513-534.
- [15] W. W. Willmarth, N. E. Hawk and R. L. Harvey, Steady and unsteady motions and wakes of freely falling disks, *Phys. Fluids*, 7 (1964), 197-208.
- [16] K. Xu, A gas-kinetic BGK scheme for the Navier-Stokes equations and its connection with artificial dissipation and Godunov method, *J. Comput. Phys.*, 171 (2001), 289-335.
- [17] K. Xu and X. Y. He, Lattice Boltzmann method and gas-kinetic BGK scheme in the low Mach number viscous flow simulations, *J. Comput. Phys.*, 190 (2003), 100-117.